



UNIVERSITY OF LEEDS

This is a repository copy of *The matching of polymer solution fast filament stretching, relaxation, and break up experimental results with 1D and 2D numerical viscoelastic simulation*.

White Rose Research Online URL for this paper:
<http://eprints.whiterose.ac.uk/74713/>

Article:

Vadillo, DC, MacKley, MR, Tembely, M et al. (5 more authors) (2012) The matching of polymer solution fast filament stretching, relaxation, and break up experimental results with 1D and 2D numerical viscoelastic simulation. *Journal of Rheology*, 56 (6). 1491 - 1516 .
ISSN 0148-6055

<https://doi.org/10.1122/1.4749828>

Reuse

See Attached

Takedown

If you consider content in White Rose Research Online to be in breach of UK law, please notify us by emailing eprints@whiterose.ac.uk including the URL of the record and the reason for the withdrawal request.



eprints@whiterose.ac.uk
<https://eprints.whiterose.ac.uk/>

20 **Abstract**

21 This paper is concerned with the comparison of two numerical viscoelastic strategies
22 for predicting the fast filament stretching, relaxation and break up of low viscosity,
23 weakly elastic polymeric fluids. Experimental data on stretch, relaxation and breakup
24 was obtained using a Cambridge Trimaster for a Newtonian solvent (DEP) and three
25 monodisperse polystyrene polymer solutions. Two numerical codes were tested to
26 simulate the flow numerically. One code used a 1D approximation coupled with the
27 Arbitrary Lagrangian Eulerian (ALE) approach and the other, a 2D axisymmetric
28 approximation for the flow. In both cases the same constitutive equations and mono
29 and multimode parameter fitting was used; thereby enabling a direct comparison on
30 both codes and their respective fit to the experimental data. Both simulations fitted the
31 experimental data well and surprisingly the 1D code closely matched that of the 2D.
32 In both cases it was found necessary to utilise a multimode approach to obtain a
33 realistic match to the experimental data. The sensitivity of the simulation to the choice
34 of constitutive equation (Oldroyd-B and FENE-CR) and the magnitude of non linear
35 parameters were also investigated. The results are of particular relevance to ink jet
36 processing and demonstrate that high shear rate, low viscosity viscoelastic polymeric
37 flows can be simulated with reasonable accuracy.

38 **1.Introduction**

39 The way in which viscoelastic fluids stretch, thin and break up is of relevance to a
40 number of technologies and these three aspects of the flow have in the past received
41 extensive scientific attention; although generally as three different individual topics.
42 The stretching of polymeric fluids in particular has received detailed experimental and
43 modeling attention in the last decade from amongst others (Anna and McKinley

44 (2001), McKinley and Sridhar (2002), Bach *et al.* (2002), Clasen *et al.* (2006)) where
45 the work has concentrated on determining the transient extensional viscosity of fluids.
46 The thinning of prestretched polymeric fluids has also been investigated
47 experimentally following pioneering experimental work by (Bazilevsky *et al.*, 1997)
48 which was subsequently modelled by (Entov and Hinch (1997)). A review by
49 McKinley (2005a) gives an authoritative account of factors that influence filament
50 thinning behaviour. Filament breakup is a delicate process and is the least well
51 characterized and modelled of the three topics amongst stretching, relaxation and
52 breakup covered by this paper.

53 Ink jet printing can involve all three elements considered above during filament
54 formation and droplet breakup (Dong *et al.* (2006), Hoath *et al.* (2009), Jang *et al.*
55 (2009)). In order to mimic elements of this complex deformation process a
56 “Cambridge Trimaster” geometry apparatus was developed specifically as a device to
57 capture aspects of the process with well-defined boundary conditions (Vadillo *et al.*
58 (2010a)). The Cambridge Trimaster has strong similarity to the single piston Rozhkov
59 filament thinning device (Bazilevsky *et al.* (1990) and the Haake Caber filament
60 thinning apparatus (<http://www.thermo.com/com/cda/product/detail/>). The twin piston
61 Trimaster was developed specifically for low viscosity fluids with a fast, controlled
62 initial displacement and for use with high speed photography [Vadillo *et al.*(2010a)].

63 Characterisation of low viscosity, linear viscoelasticity with short relaxation times is a
64 challenging area of rheology, however the Pecho, Piezo Axial Vibrator (PAV)
65 (Groß *et al.* (2002), Kirschenmann (2003), Crassous *et al.* (2005), and Vadillo *et al.*
66 (2010b)) is an apparatus that can probe fluid within the range of millisecond
67 relaxation times. Thus by using a combination of the Cambridge Trimaster and the
68 PAV it was possible to probe both the extensional filament break up behaviour of

69 viscoelastic fluids that are well characterized, at least in the Linear Viscoelastic
70 (LVE) regime using the PAV.

71 In a recent work, some authors of this paper have published the matching of
72 experimental and simulation filament stretching and thinning data using the single
73 mode Maxwell description for the viscoelastic contribution of the fluid (Tembely *et*
74 *al.* (2012). The results were promising, although all the elements of the Trimaster data
75 with a single mode 1D simulation of the process of thinning and break up could not be
76 fully captured. A direct comparison between 1D and 2D modeling may be found in
77 the work of Yildirim and Basaran (2001) and more recently by Furlani and Hanchak
78 (2011). The latter authors have used the slender jet 1D approximation and solved the
79 nonlinear partial differential equations using the method-of lines wherein the PDEs
80 are transformed to a system of ordinary differential equations for the nodal values of
81 the jet variables on a uniform staggered grid. The 1D results are impressive with the
82 key advantages being the ease of implementation and the speed of computation albeit
83 in a different configuration than the problem considered in this paper. In the present
84 paper, Trimaster data for polymer solutions are matched to single and multimode
85 viscoelastic simulation data, using both a computationally time efficient 1D
86 simulation and a potentially more rigorous 2D simulation. The paper represents a
87 “state of art” position in matching extensional time dependent results with high level
88 numerical simulation, thereby enabling the effects of constitutive equation and
89 constitutive parameters to be tested.

90 **2. Test fluids, rheological characterisation and Trimaster experimental protocols.**

91 **2a Test fluid preparation and characterisation.**

92 The fluids used were a series of mono-disperse polystyrene dissolved in diethyl
93 phthalate (DEP) solvent as previously described in [Vadillo *et al.*, 2010]. Near mono
94 disperse Polystyrene polymer was manufactured specially by Dow, and gel
95 permeation chromatography (GPC) with THF as the solvent enabled determination of
96 mass and number average molecular weights M_w and M_n as 110 kg/mol and
97 105kg/mol respectively. A stock solution of PS dilution series was prepared by adding
98 10wt% of PS to the DEP at ambient temperature. The resulting solution was heated to
99 180°C and stirred for several hours until the polymer was fully dissolved. The
100 dilution series were prepared by subsequent dilution of the respective stock solutions.
101 Sample surface tension remained constant at 37mN/m up to 10wt% PS110
102 concentration and with a critical polymer overlap concentration c^* of 2.40wt%
103 [Clasen *et al.* (2006a)]. The zero shear viscosities η_0 of the solutions were determined
104 from PAV low frequency complex viscosity η^* data within the terminal relaxation
105 regime and the measured viscosities are given in Table I.

106 **Table I:** Zero shear rate complex viscosity of the different polymer solutions at 25°C

107 **2b. Rheological characterisation.**

108 The Piezo Axial Vibrator (PAV) has been used to characterise the linear viscoelastic
109 behaviour of samples with viscosity has low as 1mPa.s on a frequency range
110 comprised between 0.1Hz and 10000Hz [Groß *et al.* (2002); Kirschenmann (2003);
111 Crassous *et al.* (2005); Vadillo *et al.* (2010b) The PAV measures the complex
112 modulus G^* of the test fluid with $G^* = G' + iG''$ and where G' is the storage modulus
113 and G'' is the loss modulus. The complex viscosity η^* is related to the complex
114 modulus by $\eta^* = G^*/\omega$ where ω is the angular frequency. Experimental LVE results
115 are presented in Fig. 1. Loss modulus G'' and elastic modulus G' have been found to

116 increase with the frequency and to vertically shift with the polymer addition. Note, the
117 pure DEP solvent does not show any G' . Both moduli approach at lower frequencies
118 the terminal relaxation regime with the expected scaling with a power of 1 for the loss
119 modulus (Fig. 1.a), and a power of 2 for the storage modulus (Fig. 1.b), and a constant
120 complex viscosity η^* in this regime as shown in Fig. 1.c (except for 5wt% PS110 after
121 2000Hz). The experimental results are displayed between 10^2 and 10^4 Hz, the range
122 on which the storage modulus has been captured. At lower frequency, the fluids have
123 been found essentially to behave as a Newtonian fluid with the presence of a loss
124 modulus only.

125 **2c. Cambridge Trimaster experimental protocol**

126 The Cambridge Trimaster (CTM) is a Capillary Breakup Extensional Rheometer that
127 has been specifically designed to probe the extensional rheology of weakly
128 viscoelastic fluids. This apparatus performs a fast stretch of a cylinder of fluid
129 initially located between two identical pistons over a short distance. This apparatus
130 and its limitation have been presented in details in [Vadillo *et al.* 2010a]. In the
131 present study, the piston diameters are 1.2mm and the experimental filament
132 stretching conditions are an initial gap size L_0 of 0.6mm and a stretching distance L_f
133 of 0.8mm at a relative piston speed $2V_p$ of 150mm/s. This corresponds to a filament
134 strain rate $2V_p/L_0 = 250 \text{ s}^{-1}$ and a filament aspect ratio L_f/L_0 of 2.3. The piston
135 velocity and stretching distance have been chosen to ensure that pistons stop their
136 motion before the critical time scale for inertio-capillary break up for the sample with
137 the lower viscosity, here the DEP. For such a fluid, this time scale has been estimated
138 around 5ms [Tembely *et al.*, 2012]. These conditions have been used in the
139 following for both experiments and simulations.

140 The transient filament profiles were captured using a Photron Fastcam
141 (http://www.photron.com/index.php?cmd=product_general&product_id=1) 1024 PCI
142 high speed camera at 6000 fps, for a picture size of 128 x 256 with a shutter time of
143 3 μ s. The filament thinning measurement, as well as the filament breakup behaviour,
144 was obtained using automatic image processing based of greyscale variation
145 throughout image for edge detection and the minimum diameter that can be resolved
146 was about $\sim 6\mu\text{m}$.

147 **2d Relaxation time and moduli determination.**

148 Relaxation spectrum determination from LVE measurements is an ill-posed problem
149 and has been studied extensively in the literature [see for example Baumgaertel and
150 Winter (1989); Kamath *et al.* (1990), Stadler and Bailly (2009)] and different
151 techniques from linear to non-linear regression have been developed to obtain
152 relaxation spectra from oscillatory LVE data. In the modelling carried out here, a
153 series of equidistant relaxation times spaced on the logarithmic scale was chosen with
154 one mode per decade. This was motivated by the fact that, in experiments, low visco-
155 elastic fluids have shown significant differences between relaxation times in shear and
156 in extension [Clasen *et al.* (2006)] and recent simulations have shown that using a
157 single mode Maxwell description of the fluid was not sufficient [Tembely *et al.*
158 (2012)] to capture those differences. The minimization program for both G' and G''
159 data was solved using Matlab $\text{\textcircled{R}}$. The solution involved the use of SQP (Sequential
160 quadratic programming) [Jorge and Wright (2006)] methods which may be considered
161 as a state of the art nonlinear programming optimization technique. This method has
162 been shown to outperform other methods in terms of accuracy, efficiency, and
163 adaptability over a large number of problems [Schittkowski (1985)] and it is an

164 effective method for non-linear optimization with constraints. In each iteration the
 165 non-linear problem was approximated using a quadratic which is easy to solve (hence
 166 the name SQP).

167 The conversion of the experimental data (G'_m, G''_m, ω_j) into a relaxation function was
 168 performed by expressing $G(t)$ as a discrete relaxation spectrum (g_i, λ_i). The Maxwell
 169 model relates the real and imaginary parts of the complex modulus determined in
 170 LVE measurement to the discrete relaxation spectrum of N relaxation times λ_i and a
 171 relaxation strengths g_i through:

$$172 \quad G'(\omega) = \sum_{i=1}^N g_i \frac{(\omega\lambda_i)^2}{1 + (\omega\lambda_i)^2} \quad (1)$$

$$173 \quad G''(\omega) = \eta_s \omega + \sum_{i=1}^N g_i \frac{\omega\lambda_i}{1 + (\omega\lambda_i)^2} \quad (1)$$

174 with ω being the angular frequency of the experiment, and N is the number of
 175 relaxation modes. As indicated in (2), G'' accounts for the solvent viscosity.

176 Generally the spectra can be computed by minimizing the “least mean square error”
 177 as follows [Armstrong *et al.* (1987); Curtiss *et al.* (1987); Stadler and Bailly (2009)]:

$$178 \quad D = \sum_{j=1}^M \left[\frac{G'(\omega_j)}{G'_m(\omega_j)} - 1 \right]^2 + \left[\frac{G''(\omega_j)}{G''_m(\omega_j)} - 1 \right]^2 \quad (2)$$

179 where M is the number of measurements.

180 The model was initialized by choosing the relaxation times to be equidistantly spaced
 181 on a logarithmic scale such that $\log(\lambda_i / \lambda_{i+1}) = 1/p$. Setting $p = 1$, i.e, one mode per
 182 decade, has been found to provide sufficient accuracy to accurately describe the LVE

183 behavior (Fig. 1). In the numerical simulation, the Maxwell component of the model
184 was fitted with 5 modes. The relaxation times are chosen such that G' and G''
185 measured over the frequency range $\omega_{\min} < \omega < \omega_{\max}$ recover all the information
186 regarding the relaxation spectrum over the range $1/\omega_{\max} < \lambda_i < 1/\omega_{\min}$, however the
187 correct range is given by $e^{\pi/2}/\omega_{\max} < \lambda_i < e^{-\pi/2}/\omega_{\min}$ [Davies and Anderssen (1997)].
188 This spectrum is a generalized form of the Maxwellian dynamics [Ferry (1980)] and
189 shown in Table II.

190 **3. General equations and numerical simulations.**

191 Numerical simulations of the Trimaster deformation were performed using both a
192 one-dimensional model and a 2D axisymmetric model. In the following sub-sections
193 the general equations and the numerical techniques used in both cases are detailed.

194 **3a. Flow geometry.**

195 To model the experimental conditions, an initial cylindrical column of fluid was
196 considered bounded by two rigid circular pistons of diameter D_0 . The fluid and the
197 pistons were initially at rest; subsequently the pistons moved vertically outwards with
198 time-dependent velocities $V_p(t)$ (top piston) and $-V_p(t)$ (bottom piston), which are
199 prescribed functions based on fitting a smooth tanh curves through measurements of
200 the Trimaster piston motion in the experiments. As described in Tembely et al 2011,
201 the form of tanh has been chosen to fit the symmetrical “S” shape experimentally
202 observed for the piston motion with time. In that work, the authors have shown that
203 the use of an accurate representation of the piston dynamic response is of importance
204 in the simulation of fast transient dynamic of low viscosity and/or low viscoelasticity
205 fluids.

206 Using a cylindrical coordinate system $\{r, \theta, z\}$, the flow was constrained to be
 207 axisymmetric so that all flow fields are independent of the angular coordinate θ , and
 208 the simulation may be restricted to the rz -plane. The coordinate origin is at the axis of
 209 the jet, midway between the initial positions of the two pistons. Fig. 2 shows a
 210 schematic diagram of the computational domain at an intermediate stage of the piston
 211 motion.

212 Symmetric boundary conditions are required along the z -axis to maintain
 213 axisymmetry, and conditions of no-slip were applied at each piston surface. The
 214 boundary conditions at the free surface are those of zero shear stress and the
 215 interfacial pressure discontinuity due to the surface curvature

$$216 \quad \underline{\mathbf{t}} \cdot \underline{\mathbf{T}} \cdot \underline{\mathbf{n}} = 0 \quad \text{and} \quad \left[\underline{\mathbf{T}} \cdot \underline{\mathbf{n}} \right]_{\text{air}}^{\text{fluid}} = -\gamma \kappa, \quad (3)$$

217 where $\underline{\mathbf{T}}$ is the total stress tensor, $\underline{\mathbf{n}}$ is the unit vector normal to the free surface
 218 (directed outward from the fluid), $\underline{\mathbf{t}}$ is the unit tangent vector to the free surface in the
 219 rz -plane, γ is the coefficient of surface tension, and κ is the curvature of the interface.
 220 It is assumed that the external air pressure is a negligible constant.

221 The location of the free surface at each time-step was determined implicitly via a
 222 kinematic condition. In the axisymmetric simulations, this was realized
 223 automatically, since the mesh is Lagrangian and the mesh nodes are advected with the
 224 local fluid velocity. The contact lines between the free surface and the pistons were
 225 held pinned at the piston edges throughout.

226 The initial conditions are that the fluid is at rest ($\mathbf{v}=\mathbf{0}$) and the polymer is at
 227 unstretched equilibrium ($\mathbf{A}_i=\mathbf{I}$).

228 **3b. Governing equations**

229 The governing equations for incompressible isothermal flow of a viscoelastic fluid are
 230 the classical Navier-Stokes equations for Newtonian fluids together with an additional
 231 viscoelastic term coming from the extra stress tensor $\underline{\underline{\sigma}}$. The momentum conservation
 232 then may be expressed as follows in which the 3rd term on right-hand-side accounts
 233 for viscoelasticity:

$$234 \quad \rho \frac{d\mathbf{v}}{dt} + \rho(\mathbf{v} \cdot \nabla)\mathbf{v} = -\nabla p + \eta_s \nabla^2 \mathbf{v} + \nabla \cdot \underline{\underline{\sigma}} + \rho g \mathbf{z} \quad (4)$$

235 and the continuity equation reads:

$$236 \quad \nabla \cdot \mathbf{v} = 0 \quad (5)$$

237 where p is the fluid pressure, ρ is the fluid density, η_s is the solvent viscosity, and g is
 238 the acceleration due to gravity.

239 **3c. Constitutive equations**

240 For the viscoelastic fluid models, the polymer contribution was described by a
 241 Finitely Extensible Nonlinear Elastic (FENE) dumbbell model which makes use of
 242 the conformation tensor \mathbf{A} , and the stress tensor reads [see for example, Chilcott and
 243 Rallison (1988)]:

$$244 \quad \underline{\underline{\sigma}} = Gf(R)(\mathbf{A} - \mathbf{I}) \quad (6)$$

245 where G is the elastic modulus, $f(R)$ is the finite extensibility factor related to the
 246 finite extensibility parameter L , representing the ratio of a fully extended polymer
 247 (dumbbell) to its equilibrium length and $R = \text{Tr}(\mathbf{A})$. L can be described in terms of
 248 molecular parameters as:

249

$$L = \sqrt{3} \left[\frac{j(\sin \theta/2)^2 M_w}{C_\infty M_u} \right]^{1-\nu} \quad (7)$$

250 In this expression, θ corresponds to the C-C bond angle and is equal to 109.5° , j
 251 corresponds to the number of bonds (2 in the case of PS) of a monomer of molar mass
 252 $M_u = 104\text{g/mol}$, C_∞ is the characteristic ratio for a given polymer equal to 9.6, M_w is
 253 the molecular weight of the polymer and ν is the excluded volume exponent equals to
 254 0.57 for PS110 [Clasen *et al.* (2006b)]. In the case where the dumbbells are infinitely
 255 extensible, $f(R) = 1$ and the constitutive equation is that of an Oldroyd-B fluid. For
 256 PS110, L has been estimated at 15.

257 For a multimode model, the extra stress may be expressed as a sum of contributions
 258 from each mode. For the generalized multimode problem with N modes, each mode
 259 (i) with partial viscosity (η_i) and relaxation time (λ_i), and the extra-stress tensor of the
 260 FENE-CR expresses:

261

$$\underline{\underline{\sigma}} = \sum_{i=1}^N g_i f_i(R_i) (\mathbf{A}_i - \mathbf{I}), \quad (8)$$

262 where $f_i(R_i) = 1 / (1 - R_i / L_i^2)$ with $R_i = \text{Tr}(\mathbf{A}_i)$. For simplicity, it is assumed that the
 263 extensibility $L_i = L$ is constant, but other approaches may be used [Lielens *et al.*
 264 (1998)]. The dimensionless evolution equation for the i^{th} mode is

265

$$\frac{d\mathbf{A}_i}{dt} = -\frac{f_i(R_i)}{\text{De}_i} (\mathbf{A}_i - \mathbf{I}), \quad (9)$$

266 Where $\overset{\nabla}{\mathbf{A}}_i = \frac{d\mathbf{A}_i}{dt} - \nabla \mathbf{v}^T \cdot \mathbf{A}_i - \mathbf{A}_i \cdot \nabla \mathbf{v}$ is the Oldroyd upper-convected time derivative of

267 \mathbf{A}_i , and De_i is the Deborah number for the i^{th} mode defined as follow

268

$$\text{De}_i = \lambda_i / \tau \quad (11)$$

269 g_i and λ_i are the moduli and relaxation times described by the multimode
 270 optimization see sub-section (2d) and where τ is the characteristic inertio-capillary
 271 time scale of the system defined by $\tau = \sqrt{\rho R_0^3 / \gamma}$.

272 Scaling was performed using the piston radius R_0 as a length scale, and a
 273 characteristic speed U as a velocity scale, where U is the average piston speed in the
 274 2D case, and $U = R_0 / \tau$ in the 1D case. The time was scaled by R_0 / U and τ , in the 2D and
 275 1D cases respectively; whereas pressures and stresses were scaled by ρU^2 . The
 276 scalings yielded the dimensionless governing equations:

$$277 \quad \frac{d\mathbf{v}}{dt} + (\mathbf{v} \cdot \nabla) \mathbf{v} = -\nabla p + \frac{1}{\text{Re}} \left(\nabla^2 \mathbf{v} - \sum_{i=1}^N c_i \nabla A_i \right) + \frac{1}{\text{Fr}^2} \mathbf{z}, \quad \nabla \cdot \mathbf{v} = 0, \quad (10)$$

278 where t , \mathbf{v} , and p are now the dimensionless time, velocity, and pressure
 279 respectively. For each viscoelastic mode an additional parameter $c_i = g_i \lambda_i / \eta_s$ has been
 280 introduced: it may be interpreted as a measure of the concentration (volume fraction)
 281 of dumbbell molecules corresponding to the i^{th} mode. With the particular scalings
 282 used here, the flow is characterized by the dimensionless groups Re , We , and Fr ,
 283 which are respectively the Reynolds, Weber, and Froude numbers

$$284 \quad \text{Re} = \frac{\rho U R_0}{\eta_s}, \quad \text{We} = \frac{\rho U^2 R_0}{\gamma}, \quad \text{Fr} = \left(\frac{U^2}{g R_0} \right)^{1/2}, \quad (13)$$

285 in addition to the Deborah number De_i for each mode, defined earlier. **The Reynolds**
 286 **number represents the competition between inertia and viscosity, the Weber number**
 287 **the competition between the inertia and the surface tension while the Froud number**
 288 **represents the competition between inertia and gravity effects.**

289 Another important dimensionless number is that of Ohnesorge, $\text{Oh} = \eta_s / \sqrt{\rho \gamma R_0}$. With
 290 the scalings used here, the Ohnesorge number can be expressed in terms of the Weber

291 and Reynolds numbers: $Oh = \sqrt{We} / Re$. Alternative choices of scaling may result in
 292 other different dimensionless groupings [Eggers and Villermaux, (2008)] as for
 293 example, the Capillary number (ratio between viscous forces and surface tension) and
 294 the Bond number (ratio between gravitational forces and surface tension). The Bond
 295 number and the Capillary number have been estimated at ~ 0.11 and between 0.04 and
 296 0.28 respectively indicating that surface tension is the dominating force and the
 297 gravitational effects negligible. An extensive discussion of dimensionless number of
 298 the problem can be found in [McKinley, 2005b].

299 3d. Computational methods

300 1D simulation

301 The previous equations (4), (5), (6) can be further simplified to retrieve the lubrication
 302 equation. The 1D simulation method follows the same approach as in the recently
 303 presented published work by Tembely *et al.* (2012) namely considering the radial
 304 expansions and taking the lower order results in r lead to the nonlinear one-
 305 dimensional equations describing the filament dynamics [Eggers and Dupont (1994);
 306 Shi *et al.* (1994)]. The result is a system of equations for the local radius $h(z, t)$ of the
 307 fluid neck, and the average velocity $v(z, t)$ in the axial direction:

$$308 \quad \partial_t h + vh' + v' \frac{h}{2} = 0 \quad (14)$$

309 where prime (') denotes the derivative with respect to z coordinates and

$$310 \quad \partial_t v + vv' = -\kappa' + 3\tilde{v}_s \frac{(v'h^2)'}{h^2} + \frac{1}{h^2} \left[h^2 (\sigma_{p,zz} - \sigma_{p,rr}) \right], \quad (15)$$

311 For the multimode one-dimensional model in dimensionless form, the axial and radial
 312 stress may be expressed as:

$$313 \quad \sigma_{p,zz} = \sum_{i=1}^N g_i f(R_i) A_{zz,i} \quad (16)$$

$$314 \quad \sigma_{p,rr} = \sum_{i=1}^N g_i f(R_i) A_{rr,i} \quad (17)$$

315 As previously, the full expression of the curvature given in equation (18) was used to
 316 avoid instability in the solution and to provide the capacity to represent a rounded
 317 drop:

$$318 \quad \kappa = \frac{1}{h(1+h'^2)^{1/2}} - \frac{h''}{(1+h'^2)^{3/2}} \quad (11)$$

319 To close the one-dimensional model, the following boundary conditions are imposed,
 320 the no-slip conditions at the piston surfaces,

$$321 \quad h(z = -L/2, t) = h(z = L/2, t) = R_0 \quad (12)$$

$$322 \quad v(z = -L/2, t) = -V_p, v(z = L/2, t) = V_p \quad (13)$$

323 and a kinematic condition for the radius $h(z, t)$ of the jet may be expressed as

$$324 \quad \frac{dh}{dt} = \frac{\partial h}{\partial t} + v_z \frac{\partial h}{\partial z} = v_r(r = h, t) \quad (14)$$

325 The governing equations in 1D simulation were solved with COMSOL,
 326 (<http://www.uk.comsol.com/>) using the Arbitrary Lagrangian-Eulerian (ALE)
 327 technique. The ALE technique is such that the computational mesh can move
 328 arbitrarily to optimize the shape of the elements, whilst the mesh on the boundaries

329 follows the pistons motion. This ALE capacity implemented in the Comsol code
330 combined with the choice of very fine meshes enables to track the relevant physics as
331 shown in (Tembely *et al.* 2012). Due to the piston motion the computational domain
332 changes with time (see Fig. 3). With the ALE approach, the time derivative of any
333 quantity is defined as $\frac{d}{dt} = \frac{\partial}{\partial t} + (\vec{v} - \vec{v}_m) \cdot \nabla$

334

335 where \vec{v}_m is the mesh velocity imposed by the piston velocity.

336 The stress boundaries are ignored in the 1D approach due to the weakly viscoelastic
337 character of the samples and the initial filament aspect ratio being close to 1 [Yao and
338 McKinley, 1998]. The 2D axisymmetric approach includes *per se* that effect.

339 Fig. 4 presents the evolution of the simulated mid-filament as a function of time for
340 1D and 2D simulation using different number of mesh elements. The 1D numerical
341 results with between 240 and 3840 mesh elements do not show any difference. The
342 results thus seem to be insensitive to mesh size as shown in the figure below. Similar
343 observation is made for the 2D simulation results regardless of the initial number of
344 mesh elements. The 2D simulation approach mesh is adaptive and evolves with time
345 throughout the simulation resulting a very large number of elements (see insert in Fig.
346 4.a).

347

348 **2D simulation**

349 An extended version of the split Lagrangian-Eulerian method of Harlen *et al* [Harlen
350 *et al.* (1995)] was used. The nature of the extension was twofold: in the problems for
351 which the method was originally developed there were no free surface boundaries,
352 and the inertial terms were neglected ($Re = 0$). The method has since been adapted
353 and extended to deal with inertial flows and has been used to model the breakup of

354 Newtonian and viscoelastic jets [Morrison and Harlen (2010); Castrejon-Pita *et al.*
355 (2011)].

356 The velocity and pressure fields are discretized over an irregular triangular mesh of
357 P_1 - P_1 Galerkin elements; each component of the conformation tensor \mathbf{A} is assigned
358 a value for each element. An artificial stabilization was employed in order to prevent
359 spurious numerical pressure oscillations [Brezzi and Pitkaranta (1984)]. The value of
360 the stabilization parameter was optimized with respect to the spectral properties of the
361 discrete coefficient matrix [Wathen and Silvester (1993)]. A theta-scheme was used
362 for the discrete time-stepping, and the discrete governing equations were linearized
363 via Picard iteration. For each iteration, the linear system was solved numerically using
364 the minimal residual (MINRES) method [Paige and Saunders (1975)]. Adaptive time-
365 stepping was controlled by a CFL [Courant *et al.* (1928)] condition. The position of
366 each mesh node was updated after each time-step using the converged velocity
367 solution.

368 The numerical integration of the evolution equation for the conformation tensor was
369 conducted separately for each element between time-steps, by transforming to a co-
370 deforming frame with local coordinates in each triangle. In such a frame, the upper
371 convected derivative $\overset{\nabla}{\mathbf{A}}$ becomes the ordinary time derivative $d\mathbf{A}/dt$. Similarly the
372 Lagrangian derivative $D\mathbf{u}/Dt$ becomes $d\mathbf{u}/dt$. The interfacial boundary condition is
373 handled similarly to the treatment by [Westborg and Hassager (1989)].

374 To maintain element shape quality throughout the simulations, local mesh
375 reconnections were made between time-steps in regions where significant element
376 distortion had occurred. The criteria for reconnection were based on the geometric
377 optimality of the Delaunay triangulation [Edelsbrunner (2000)]. The local mesh

378 resolution was also maintained by the addition of new nodes in depleted regions, and
379 the removal of nodes in congested regions.

380 In order to represent the capillary breakup of thin fluid filaments, the fluid domain
381 was subdivided artificially when the filament radius falls below a certain threshold.
382 This threshold has been taken as $< 0.5\%$ of the piston diameter to match the smallest
383 diameter that can be experimentally resolved ($\sim 6\mu\text{m}$). Below this value, the filament
384 is not experimentally visible and is therefore considered broken. A more detailed
385 discussion of the capability of the simulations to capture pinch-off dynamics on a
386 finer scale is given in [Castrejon-Pita *et al.* (2011)].

387

388 **4. Results and discussion**

389 **4.a Experimental results**

390 Examples of the base experimental data are shown in Fig. 5 where photographs of
391 Trimaster experiments for different polymer loading are shown as a function of time.
392 The pure DEP solvent, shown as series 5a, indicates a filament stretch followed by
393 end pinching during relaxation to give a single central drop. The other extreme is
394 shown by series 5d for the 5% polymer loading, where stretching is followed by a
395 progressive filament thinning with a very much longer break up time. The whole time
396 evolution of the full profile along the thread is of general interest and importance;
397 however the detailed behaviour of the centre line diameter will be considered
398 beforehand.

399 **4.b Numerical results**

400 **Mid filament evolution**

401 The experimental time evolution of the mid-point of the filament is given in Fig. 6
402 and the figure displays the characteristic feature of an increased filament life time
403 with a progressive increase of polymer loading. It is this experimental mid filament
404 time evolution that has been used as the basis for comparison with the 1D and 2D
405 numerical simulations. Fig. 7 shows that both the 1D and 2D numerical simulations
406 are in close agreement with the base case Newtonian experimental results. Both the
407 decay profile and final 7.5 ms break point are accurately described by the simulations.
408 Figures 7 to 15 present the evolution of the mid-filament and not the minimum
409 filament or the breakup point which position might vary from one case to another.
410 The simulation breakup diameter has been set at $6\mu\text{m}$ but might occur at the top and
411 bottom of the filament, as experimentally observed in the case of DEP. In such case,
412 a droplet is formed in the middle of the filament explaining the large diameter
413 observed experimentally and in simulations at breakup time (Fig. 5 and 7).

414 Single mode simulations are shown in Fig. 8, 9 and 10 for 1, 2.5 and 5%
415 concentration solutions respectively. The simulations were carried out using the
416 FENE-CR constitutive equation with the extensibility parameter $L = 30$. The
417 extensibility value of $L = 30$ adopted in this paper has been found to provide a better
418 match with the experimental results than the theoretical value of 15. The possible
419 existence of higher molecular mass chains, albeit in small quantities, may justify this
420 choice. Moreover, for an indication of the choice of L , the comparative plot depicted
421 in Fig 13.b of the squared extensibility L^2 and $R_i = \text{Tr}(\mathbf{A}_i)$, which represents the
422 average length per mode i.e. of the polymer chain, shows that an extensibility value of
423 around 30 is an appropriate choice. The 5th mode seems to capture the polymer global
424 chain unravelling mechanism which takes place at larger length scales. On the other

425 hand, the others modes (1, 2, 3) with negligible values of R_i involves local changes of
426 the molecular conformation; the R_i axial evolution confirms that higher stretching
427 occurs in the middle of the filament.

428 The capillary thinning of viscoelastic fluid is controlled by the longest relaxation time
429 with a mid-filament diameter decreasing in the form of $D(t) \sim \alpha \cdot \exp(-t/3\lambda)$
430 [Bazilevsky *et al.* (1990)]. Fitting this exponential decay to the experimental data
431 presented in Fig. 6 yields extensional relaxation times λ_{ext} of 0.425ms, 1.19ms and
432 3.2ms for 1, 2.5 and 5wt% respectively. The extensional relaxation λ_{ext} increased with
433 polymer loading as expected. Whilst both the 1D and 2D simulations match the 1%
434 solution data shown in Fig. 8, there is a progressive mismatch in both decay and pinch
435 off with increasing concentration shown in Fig. 9 and 10. In particular the decay
436 immediately after piston cessation is over predicted by both 1D and 2D simulations.
437 Perhaps surprisingly, both the 1D and 2D simulations give a similar response. It was
438 speculated that differences may appear between single mode and multimode models
439 because of the existence of shorter and longer modes and of their interactions close to
440 capillary pinch-off in the vicinity of both pistons [Matallah *et al.* (2007)].

441 In the 1D paper, (Tembely *et al.*, JOR 2012) single mode modelling only was used;
442 however both a short mode obtained from the PAV data and a long mode obtained
443 from matching with experiment were used. In that paper it was shown that the
444 smallest relaxation time as input in a non-linear model was unable to correctly predict
445 filament thinning whilst the longest relaxation time gave reasonable filament thinning
446 results but a large discrepancy with the experimental G' and G'' data. In this paper,
447 incorporation of multi modes has been carried out in order to fit with greater accuracy
448 the filament thinning experimental results whilst also capturing the PAV data too. We

449 have chosen 5 modes in order to have one mode per decade over the range of interest
450 covered experimentally. The exact choice of the number of modes is a matter of taste.
451 Two would be too few and eight probably too many.

452 In this paper, we have used the same non-linear constitutive equation as in the
453 previous paper and the the oscillatory linear viscoelastic data was then fitted to a
454 multimode model with five modes spaced by a decade between modes and the fitted
455 parameters are given in Table II. These multimode parameters were then used in both
456 the 1D and 2D simulations using the multimode FENE-CR constitutive equation (eq.
457 9 and 10). The results are shown in Fig. 11, 12 and 14 for the 1, 2.5 and 5% solutions
458 respectively. The fit at all concentrations is now greatly improved from the single
459 mode simulations over the whole decay and again there appears to be little difference
460 between the 1D and 2D simulations.

461 Using a multimode Maxwell model approach allows better accounting for the
462 transition between visco-capillary thinning and elasto-capillary thinning as shown by
463 the large reduction of the filament diameter at times between 7 and 10ms. This was
464 one of the main limitations for the single mode Maxwell approach as shown in the
465 previous section and recently reported results by some authors of this paper (Tembely
466 *et al.* (2012)). The results shown I this current paper clearly demonstrate that a
467 multimode description of the fluid is necessary and that, perhaps surprisingly, the 1D
468 simulation appears to give a closer match to the experimental results. The multimode
469 approach also captures the results for potential non-linear elongation behavior and
470 relaxation time changes with the help of using the linear time spectrum and the non
471 linear constitutive equation.

472 The sensitivity of the filament thinning and breakup to constitutive equation and non
473 linear parameters is shown in Fig. 14 and 15. In Fig. 14 it can be seen that using the

474 1D simulation, there is little difference between the multimode FENE-CR and
475 Oldroyd model predictions. Any differences that may appear were essentially masked
476 by the use of multi modes. Simulation using the theoretically predicted value for the
477 limiting extensibility L of PS110 ($L = 15$), the “best fit” obtained ($L = 30$) and a
478 significantly larger value, here $L = 100$, have been chosen to investigate the effect L
479 of the FENE-CR model. Fig. 14 shows that L does effect the simulation slightly in
480 the transition zone for the short time modes and particularly in the final stages of
481 decay with a pinch off time that decreases with decreasing limiting extensibility
482 parameter L .

483 **Transient profiles**

484 Figure 16 and 17 present the 1D and 2D multi modes FENE-CR and Oldroyd-B full
485 simulated transient profiles for the case of 5wt% PS110 diluted in DEP. A generally
486 good match between simulations is observed with differences only appearing towards
487 the end of the filament thinning mechanism, ie, near to break up. Figure 16 shows
488 that the 1D simulation predicts a final thread like decay, whereas the 2D simulation
489 still has a pinch off component. The multi mode Oldroyd-B simulations shown in
490 Figure 17 also shows a similar trend, with the 1D having a more thread like final
491 decay. Despite the improvement provided by the use of multi modes approach instead
492 of the single mode approach, these results clearly highlight the need for investigating
493 other constitutive equations for the modelling of fast stretching and filament thinning
494 of low viscoelastic fluids.

495 Detailed full profile comparison between experimental transient profiles of PS110 at
496 5wt% in DEP with FENE-CR multi modes 1D and 2D simulation transient profiles is
497 presented in Fig. 18. Both simulation approaches provide a good match with the
498 experimental profiles for the overall mechanism with again the main discrepancies

509 appearing at the late stage of the filament thinning mechanism. Close examination of
500 the experimental and simulated profiles show that the fluid regions attached to the top
501 and bottom pistons are smaller experimentally than for both simulations. This results
502 in a larger length of the thinning filament in the experimental case and may explain
503 the differences observed between 1D and 2D simulations. The filament aspect ratio is
504 usually defined by the variation between initial and final position of the piston but it
505 can be seen here that despite using similar piston motions for the simulations and the
506 experiments, differences in the filament length arise. Such filament length variations
507 are expected to significantly affect the filament break up profile especially in the case
508 of low viscosity low viscoelastic fluids. The investigation of the full velocity field, in
509 terms of simulation and using Particle Image Velocimetry (PIV) experiments, within
510 both the filament and the piston region would help the understanding of the
511 differences observed in the filament shape especially toward the break up time.

512

513 **Weissenberg number W_i and apparent extensional viscosity $\eta_{e,app}$**

514 Figure 19 presents the evolution of the Weissenberg number W_i as a function of the
515 filament thinning Hencky strain ε in the case of multi mode FENE-CR simulations.
516 Weissenberg number and filament thinning Hencky strain may be defined as follows:

517
$$W_i = \lambda_{ext} \cdot \dot{\varepsilon} \quad (22)$$

518
$$\varepsilon = 2 \cdot \ln \left(\frac{D_0}{D(t)} \right) \quad (23)$$

519
$$\dot{\varepsilon} = \frac{2}{D(t)} \frac{dD(t)}{dt} \quad (22)$$

520 The simulated data of the mid filament evolution have been used to estimate the
521 longest extensional relaxation time and value of 2.98ms and 5.1ms were obtained for

522 the 1D approach and the 2D simulation respectively, in the case of PS110 at 5wt% in
523 DEP.

524 In the case of the multimode FENE-CR approach, the 1D simulation approach
525 predicts reasonably well the overall mechanism with; in particular the double curved
526 behaviour experimentally observed in the transition between visco-capillary and
527 elasto-capillary regimes ($W_i = 0.5$) whereas the 2D approach provides a good match
528 on the long time scale but does not capture the double curvature. The behaviour at
529 high Hencky strain is correctly represented for both types of simulations.

530 The use of the multimode approach does significantly improve the match with
531 experimental data in comparison to that of the single mode and, even if all the
532 subtleties of the complex filament thinning mechanism seem not to be fully
533 represented, it provides good agreement with experimental data. The description of a
534 Weissenberg number, when using a multimode approach, has difficulties in relation to
535 a suitable choice of relaxation time used in the definition of the Weissenberg number.
536 It is also very sensitive to noise (simulation or experimental) due to the fact that it is
537 based on the derivative of the mid filament evolution.

538 Finally, Fig. 20 presents the transient apparent extensional viscosity $\eta_{e,app}$, with

539 $\eta_{e,app} = -\sigma \cdot \frac{dt}{dD_{mid}(t)}$, as a function of Hencky strain for multimode FENE-CR. The

540 comparison is particularly good in view of the approximations which have been made
541 for the calculation of the phenomenological Maxwell times. Notably, the complex
542 behaviour of the extensional viscosity is qualitatively correctly predicted at
543 intermediate times by both the 1D and 2D simulations with the prediction of the
544 sudden increase in η_{ext} after the pistons have stopped. Close attention shows that the
545 1D simulation approach produces a surprisingly good agreement with experimental

546 results, while the 2D simulation approach fails to represent the long term extensional
547 viscosity behaviour.

548

549 **5. Conclusions**

550 Results described in this paper have shown that a multimode constitutive equation
551 approach is necessary to describe the detailed viscoelastic extensional flow behaviour
552 of dilute or semi dilute polymer solutions. The result is consistent with the findings of
553 Entov and Hinch (1997) who also found it necessary to resort to a multimode mode
554 approach for higher viscosity viscoelastic polymer solutions. However, simulations
555 for different polymer concentrations indicate that the improvement due to the use of
556 multimodes instead of single mode is reduced with increase of the solution diluteness.

557 Results presented in this work indicate great potential for the simulation of very fast
558 break up dynamic of more dilute polymer solution using multimode Maxwell
559 approach with important application potential in areas such as ink jet printing.

560 The FENE-CR constitutive equation appears to be an effective suitable constitutive
561 equation to use for the fluids examined in this paper, although the Oldroyd model was
562 found to give an equivalent response when used with multimodes. It appears that
563 multimode modelling can disguise certain limiting features of different constitutive
564 models, but however remains necessary even for the monodisperse polymer systems
565 which have been tested.

566 An initially surprising result of the paper is the fact that the 1D modelling gives
567 apparently improved results over the more rigorous 2D modelling in some limited
568 cases described above. This indicates that the 1D approximation is valid enough for

569 the initial and boundary conditions used and in particular for the mid filament
570 diameter evolution. It is probable that when details of highly non-linear behaviour, i.e.
571 pinch off position, number of beads, etc. are considered differences will emerge from
572 the two techniques. The pinch off position and the number of small drops is an
573 essential parameter in ink-jet printing since the satellite drops may merge or not
574 following the type of detachment.
575 Further comparison would be to follow the filament transients following breakup.
576 Such a work has been done for Newtonian liquid (Castrejon Pita et al. 2012) but this
577 work does not include non-Newtonian fluids., The non-linear evolution of main drop
578 and satellites do influence printability criterion taking into account the Ohnesorge and
579 the Deborah numbers as described in preliminary work by Tembely et al. 2011.

580

581 **Acknowledgements**

582 DV, MRM, OGH and NFM would like to acknowledge the financial support of the
583 EPSRC and Industrial Ink Jet Consortium funding. We would also like to
584 acknowledge with thanks rheological assistance from Dr Kathryn Yearsley and thanks
585 to Inca Ltd for allowing DV to complete this paper. MT and AS wish to acknowledge
586 financial support from ANR PAN'H 2008 CATIMINHY project.

587

588

590 **References**

- 591 Armstrong R. C. and O. Hassager, Wiley, "Fluid Dynamics ", [Dyn. Pol. Liquids](#), Vol.
592 1, , (1977, 2nd ed. 1987).
- 593 Anna, S. L., and G. H. McKinley, "Elasto-capillary thinning and breakup of model
594 elastic liquids," [J. Rheol.](#)45, 115–138 (2001).
- 595 Bach, A., H. K. Rasmussen, P-Y. Longin, and O. Hassager, "Growth of non-
596 axisymmetric disturbances of the free surface in the filament stretching rheometer:
597 Experiments and simulation," [J. Non-Newtonian Fluid Mech.](#) 180, 163–186 (2002).
- 598 Bazilevsky A. V., V. M. Entov and A.N. Rozhkov, "Liquid filament microrheometer
599 and some of its applications", [Third European Rheol. Conf.](#), (Ed. D.R. Oliver)
600 Elsevier Applied Science, 41-43 (1990)
- 601 Bazilevsky A.V., V.M. Entov and A.N. Rozhkov, "Failure of polymer solutions
602 filaments", [Pol. Sc. Series B](#), **39**, 316-324 (1997)
- 603 Bhat, P. P., S. Appathurai, M. T. Harris, M. Pasquali, G. H. McKinley, and O. A.
604 Basaran, "Formation of beads- on-a-string structures during break-up of viscoelastic
605 filaments," [Nat. Phys.](#) 6, 625–631 (2010).
- 606 Castrejon-Pita, J. R., N. F. Morrison, O. G. Harlen, G. D. Martin, and I. M.
607 Hutchings, "Experiments and Lagrangian simulations on the formation of droplets in
608 continuous mode," [Phys. Rev. E](#) 83, 016301 (2011).
- 609 Castrejon-Pita, A. A., J.R.Castrejon-Pita and I.M. Hutchings, "Breakup of liquid
610 filaments", [Physic Review Letter](#), 108, 074506 (2012)
- 611 Chilcott, M. D., and J. M. Rallison, "Creeping flow of dilute polymer solutions past
612 cylinders and spheres," [J. Non-Newtonian Fluid Mech.](#) 29, 381–432 (1988).

613 Clasen C., J.P. Plog, W.-M Kulicke, M. Owens, C. Macosko, L.E. Scriven, M. Verani
614 and G.H. Mckinley, "How dilute are dilute solutions in extensional flows?", [J. Rheol.](#),
615 **50(6)**, 849-881 (2006a)

616 Clasen, C., J. P. Plog, W.-M.Kulicke, M. Owens, C. Macosko, L. E. Scriven, M.
617 Verani, and G. H. Mckinley, "How dilute are dilute solutions in extensional flows?,"
618 [J. Rheol.](#) 50(6), 849–881 (2006b).

619 Courant R., K. Friedrichs and H. Lewy, "Über die partiellenDifferenzengleichungen
620 der mathematischenPhysik", *Math. Ann.* 100 32-74 (1928)

621 Crassous, J., R. Re'gisser, M. Ballauff, and N. Willenbacher, "Characterisation of the
622 viscoelastic behaviour of complex fluids using the piezoelastic axial vibrator," [J.](#)
623 [Rheol.](#)49, 851–863 (2005).

624 Curtiss C. F., R. C. Armstrong, and O. Hassager, Wiley, " Kinetic Theory", [Dyn. Pol.](#)
625 [Liquids](#), Vol. 2 (1977, 2nd ed. 1987).

626 Dong H., W.W. Carr and J.F. Morris, "An experimental study of drop-on-demand
627 drop formation", [Phys. Fluids](#), **18**, 072102-1/072102-16 (2006)

628 Eggers J., "Nonlinear dynamics and breakup of free-surface flows", [Rev. Mod. Phys.](#),
629 **69**, 865-929 (1997)

630 Eggers, J., and T. F. Dupont, "Drop formation in a one-dimensional approximation of
631 the Navier-Stokes equation," [J. Fluid Mech.](#) 262, 205 (1994).

632 Entov V.M. and E.J. Hinch, "Effect of a spectrum relaxation times on the capillary
633 thinning of a filament elastic liquids", [J. Non-Newtonian Fluid Mech.](#), **72**, 31-53
634 (1997)

635 Ferry, J. D., *Viscoelastic Properties of Polymers* (John Wiley & Sons Inc., 1980).

636 Fontelos, M. A., and J. Li, “On the evolution and rupture of filaments in Giesekus and
637 FENE models”, *J. Non-Newtonian Fluid Mech.* 118, 1–16 (2004).

638 Furlani E.P. and M. S. Hanchak, "Nonlinear analysis of the deformation and breakup
639 of viscous microjets using the method of lines", E. P. Furlani & M. S. Hanchak, *Int. J.*
640 *Numerical Methods in Fluids* 65(5), 563-577 (2011)

641 Furlani E.P., "Temporal instability of viscous liquid microjets with spatially varying
642 surface tension", *J. Phys. A: Math. Gen.*, **38**, 263 (2005)

643 Graessley, W. W., “Polymer chain dimensions and the dependence of viscoelastic
644 properties on the concentration, molecular weight and solvent power,” *Polymer* **21**,
645 258–262 (1980)

646 Groß, T., L. Kirschenmann, and W. Pechhold, “Piezo axial vibrator (PAV)—A new
647 oscillating squeeze flow rheometer,” in *Proceedings Eurheo* edited by H. Munsted, J.
648 Kaschta, and A. Merten (Erlangen, 2002).

649 Hoath S.D., G.D. Martin, T.R. Tuladhar, M.R. Mackley, I. Hutching and D. Vadiello,
650 “Link between ink rheology, drop-on-demand jet formation and printability“, *J.*
651 *Imaging Sci. Tech.* (in press), **53**, **4**, 041208–041208-8 (2009).

652 Jang D., D. Kim and J. Moon, “Influence of fluid physical properties on ink-jet
653 printability”, *Langmuir*, **25**, 2629-2635 (2009)

654 Kamath V. and M.R. Mackley., “The rheometric characterization of flexible chain and
655 liquid crystal polymers”, 3rd European Rheology Conf., British Society of Rheology,
656 Ed. D.R. Oliver, 261-264, (1990).

657 Kirschenmann, L., Ph.D. thesis, Institut für dynamische Materialprüfung (IdM),
658 University of Ulm, (2003).

659 Matallah, H., K. S. Sujatha, M. J. Banaai, and M. F. Webster, “Single and multi-mode
660 modelling for filament stretching flows,” *J. Non-Newtonian Fluid Mech.* 146, 92–113
661 (2007).

662 McKinley G.H and G.H. and Sridhar T., “Filament Stretching Rheometry of Complex
663 Fluids”, *Annual Rev. Fluids Mech.*, **34**, 375-415 (2002)

664 McKinley G.H., “Visco-Elastic-Capillary thinning and break-up of complex fluid”,
665 *Rheology Reviews 2005, The British Soc. Rheol.*, 1-49 (2005a)

666 McKinley G.H, “Dimensionless groups for understanding free surface flows of
667 complex fluids”, *Soc. Of Rheo. Bulletin*, (2005b)

668 Morrison, N. F. and O. G. Harlen, “Viscoelasticity in inkjet printing,” *Rheol. Acta*,
669 49, 619–632 (2010).

670 Orr N.V., T. Sridhar, “Probing the dynamics of polymer solutions in extensional flow
671 using step strain rate experiments”, *J. Non-Newtonian Fluid Mech.*, **82**, 203-232
672 (1996)

673 Jang D., D. Kim and J. Moon, “Influence of fluid physical properties on ink-jet
674 printability”, *Langmuir*, **25**, 2629-2635

675 Rodd, L.E., T.P. Scott, J.J. Cooper-White and G.H. McKinley, “Capillary Breakup
676 Rheometry of Low-Viscosity Elastic Fluids”, *Appl. Rheol.*, **15** (1), 12-27, (2005).

677 Tembely M., D.C. Vadillo, M.R. Mackley and A. Soucemarianadin, “The matching of
678 a “one-dimensional” numerical simulation and experiment results for low viscosity

679 Newtonian and non-Newtonian fluids during fast filament stretching and subsequent
680 break-up”, *J. Rheol.* 56, 159-184 (2012)

681 Moussa Tembely¹, Damien Vadillo², Malcolm R. Mackley² and Arthur
682 Soucemarianadin¹, “Towards an Optimization of DOD Printing of Complex Fluids
683 , Non Impact Printing Conference, Salt Lake City, Utah (2011)

684 Vadillo, D. C., T. R. Tuladhar, A. C. Mulji, S. Jung, S. D. Hoath, and M. R. Mackley,
685 Evaluation of the inkjet fluid’s performance using the ‘Cambridge Trimaster’ filament
686 stretch and break-up device,” *J. Rheol.* 54(2), 261–282 (2010a).

687 Vadillo, D. C., T. R. Tuladhar, A. Mulji, and M. R. Mackley, “The rheological
688 characterisation of linear viscoelasticity for ink jet fluids using a piezo axial vibrator
689 (PAV) and torsion resonator (TR) rheometers,” *J. Rheol.* 54(4), 781–799 (2010b).

690 Yao M. and G.H. McKinley, “Numerical simulation of extensional deformations of
691 viscoelastic liquid bridges in filament stretching devices”, *J. Non-Newtonian Fluid
692 Mech.*, 74, 47-88 (1998).

693 Yildirim, O. E., and O. A. Basaran, “Deformation and breakup of stretching bridges
694 of Newtonian and shear- thinning liquids: Comparison of one- and two-dimensional
695 models,” *Chem. Eng. Sci.* 56(1), 211–233 (2001).

696

697

Solvent	M _w (g/mol)	C (wt%)	□* (mPa.s)
DEP	110000	0	10
DEP	110000	1	15.2
DEP	110000	2.5	31.5
DEP	110000	5	69

698 Table I: Zero shear rate complex viscosity of the different polymer solutions at 25°C

699

700

	1%PS	2.5%PS	5%PS	10%PS
i_i(μs)	g _i (Pa)	g _i (Pa)	g _i (Pa)	g _i (Pa)
1	7.789	83.8229	397.9015	1086.4419
10	428.76	1450.8952	4680.9517	9126.8723
100	1.6435	10.5177	93.1172	2012.6511
1000	0	0	0	16.4133
10000	0.0342	0.1855	0.4288	0.4291

701 Table II: Relaxation time and shear modulus obtained from Maxwell model fit of the

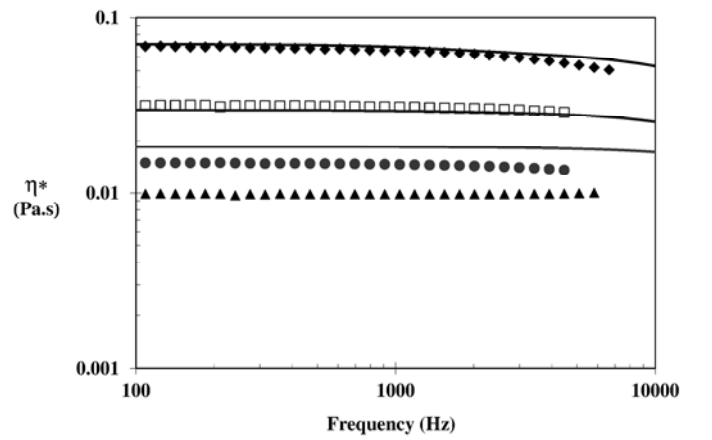
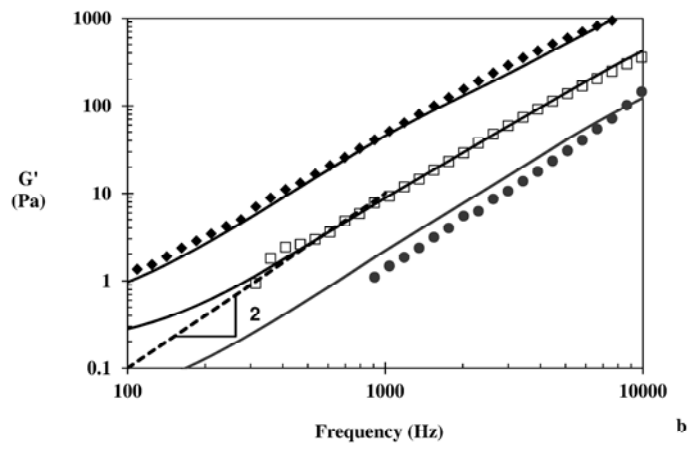
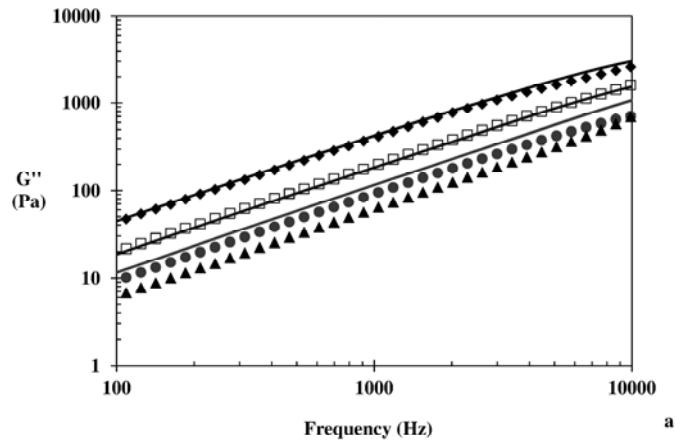
702 PAV data for the different samples

703

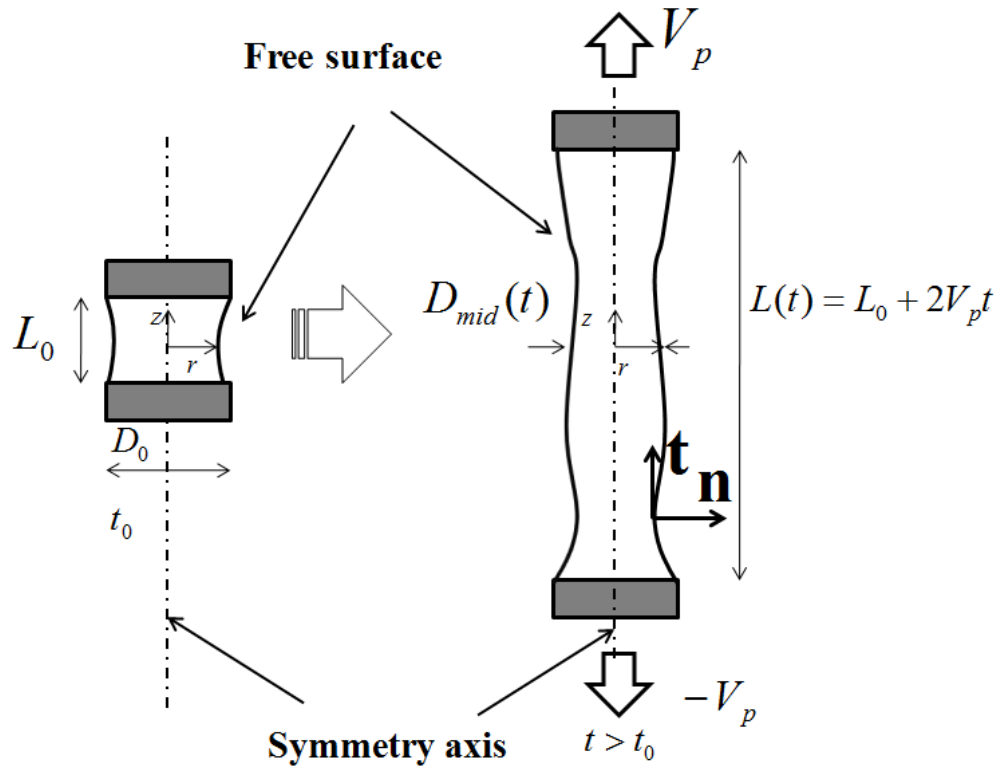
704

705

706



708 **Figure 1:** Evolution of (a) Loss modulus G'' , (b) elastic modulus G' and (c) complex
709 viscosity h^* as a function frequency for DEP-PS 110 000 solutions at different
710 concentrations. (\blacktriangle) DEP, (\bullet)DEP-1wt% PS110, (\square) DEP-2.5wt% PS110, and (\blacklozenge)
711 DEP-5wt% PS110. Solid line represents the multimode optimization results while the
712 dashed line on G' graph corresponds to a power law function of index 2.
713

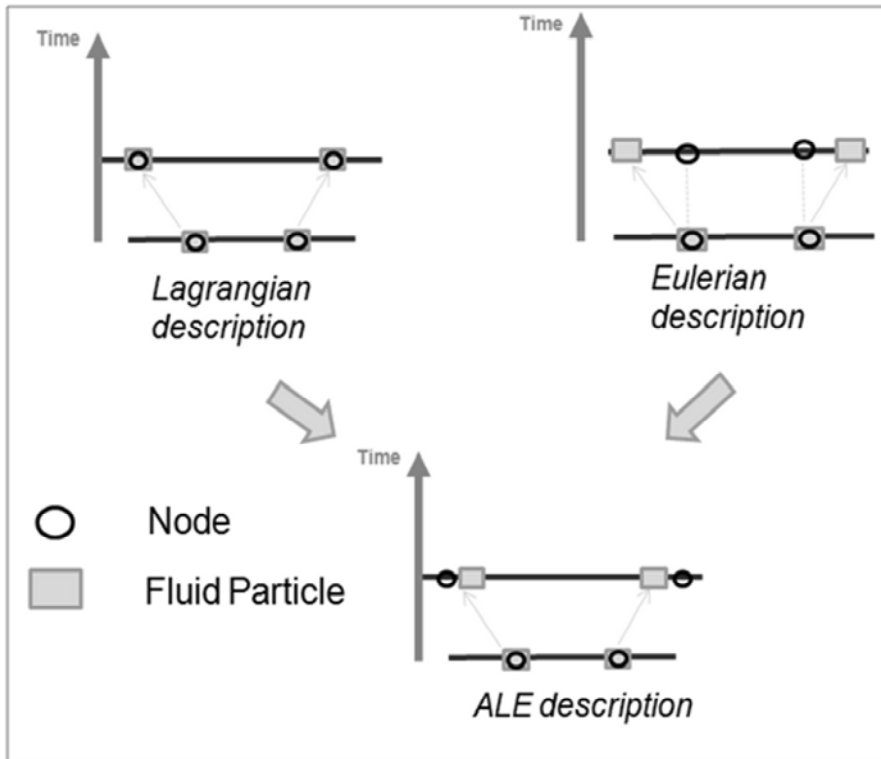


714
715

716 **Figure 2:** Diagram of filament stretch and thinning geometry and the computational
717 domain, shown midway through the stretching phase as the pistons move outwards
718 and the fluid column necks in the middle. Initially the fluid column is cylindrical.

719 **Extracted from [Tembely *et al.*, 2012]**

720
721



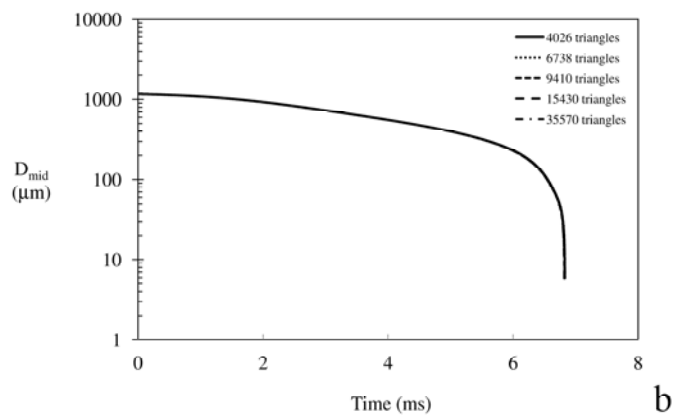
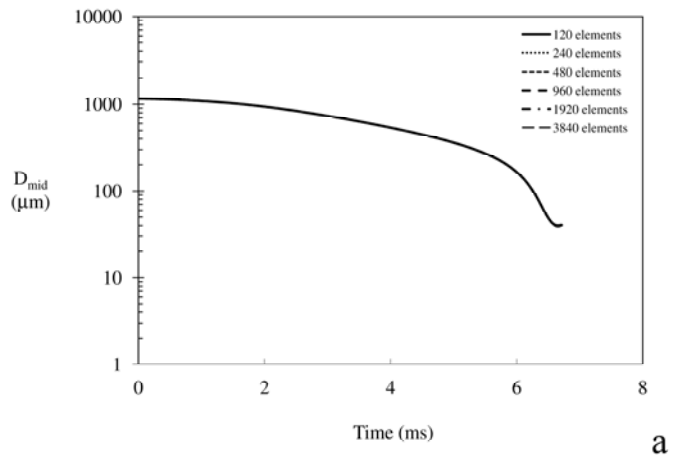
722

723

724 **Figure 3:** mesh evolution of the ALE method for the 1D simulation

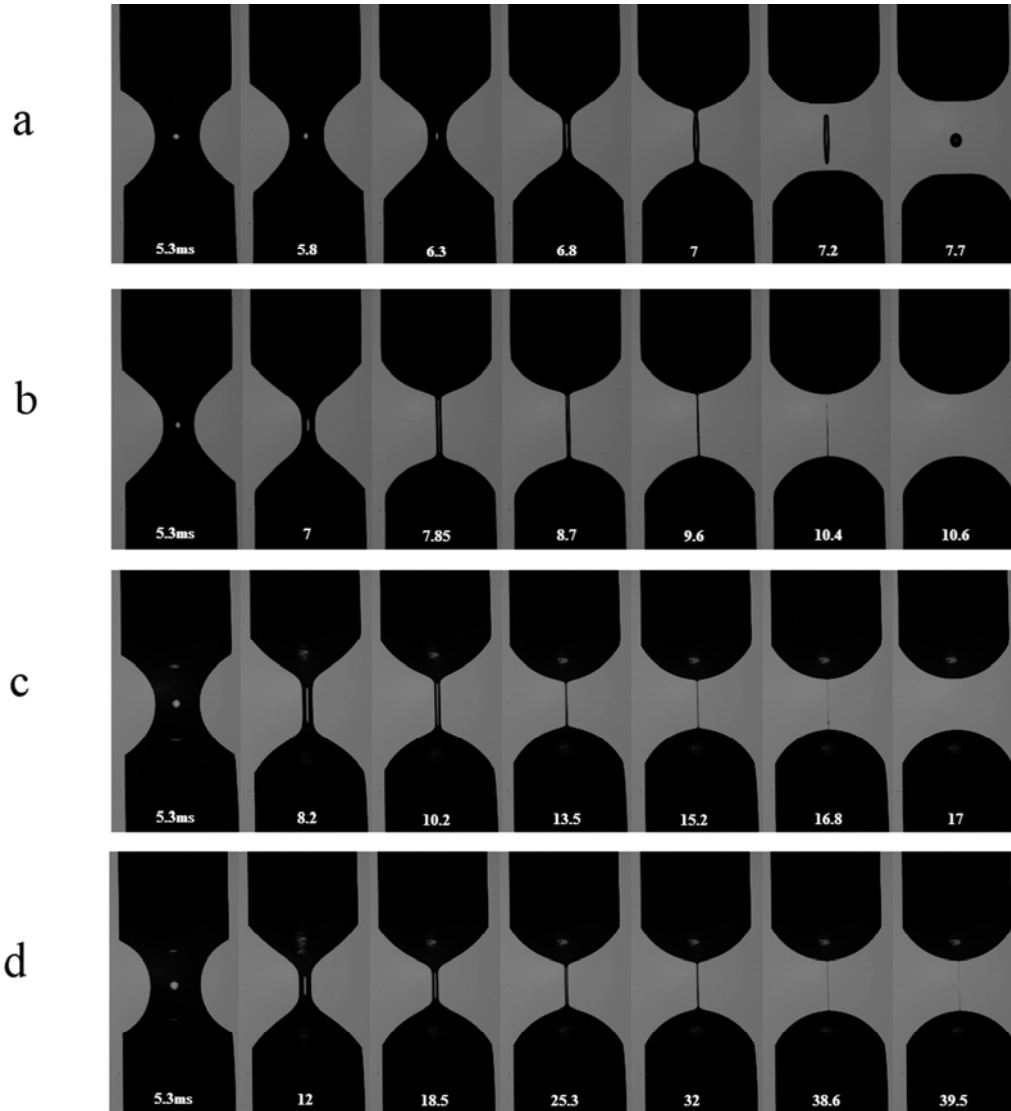
725

726



727
 728
 729
 730
 731
 732

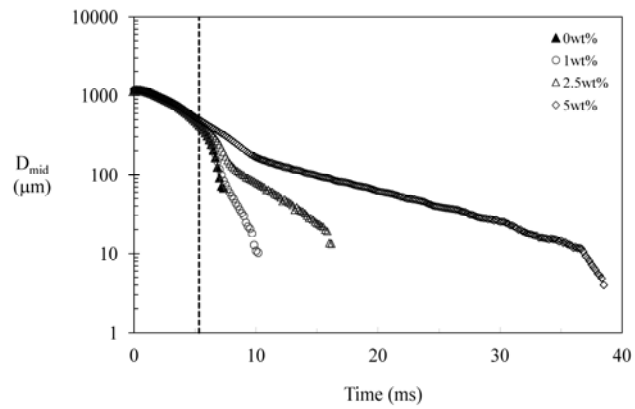
Figure 4: Evolution of the simulated mid-filament for different number of mesh elements for (a) 1D simulation approach (b) 2D simulation approach. In the 2D simulation, the legend gives the number of triangles at $t = 7.2$ ms.



734

735 **Figure 5:** Photograph of the filament stretch, thinning and break up captured with the
 736 Trimaster for (a) DEP, (b) DEP + 1wt% PS110, (c) DEP + 2.5wt% PS110, (d) DEP +
 737 5wt% PS110. The first picture of each series ($t = 5.3\text{ms}$) corresponds to the piston
 738 cessation of motion

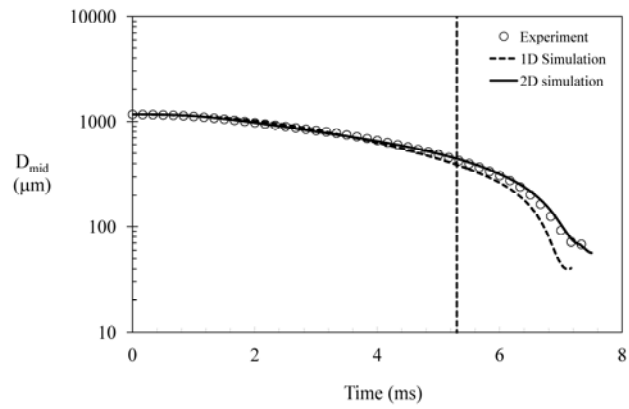
739



740
741

742 **Figure 6:** Time evolution of mid-filament taken from photographs of figure 2. (\blacktriangle)
743 DEP, (\circ) DEP-1wt% PS110, (Δ) DEP-2.5wt% PS110, and (\diamond) DEP-5wt% PS110, (---
744) piston cessation of motion.

745
746



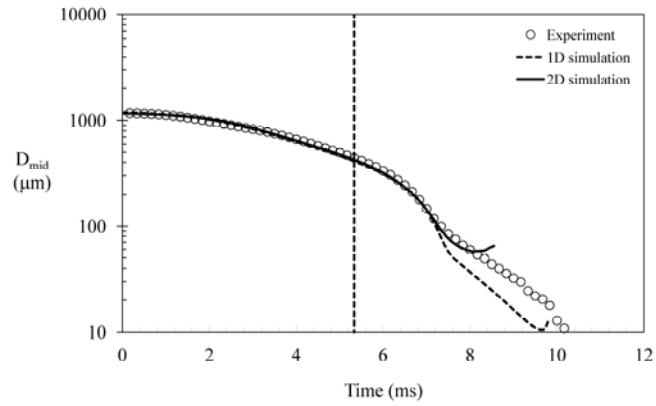
747

748 **Figure 7:** Newtonian base case. Plot of the mid filament diameter evolution as a

749 function of time. Vertical line (---) corresponds to piston cessation of motion.

750

751



752

753 **Figure 8:** Single mode, 1wt% PS110 in DEP solution. Plot of the mid filament

754 diameter evolution as a function of time. Constitutive equation: Fene-CR, relaxation

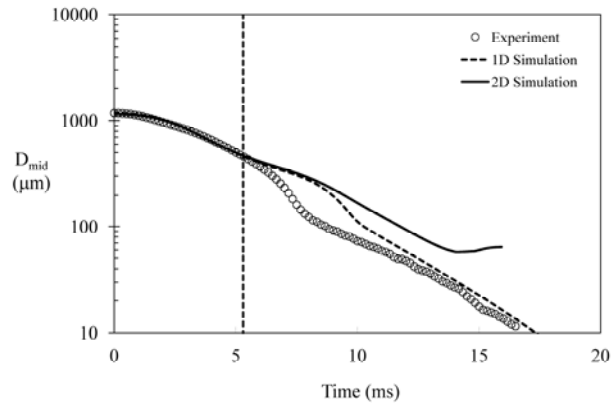
755 time $\lambda = 0.425\text{ms}$, shear modulus $g = 11.25\text{Pa}$ and polymer extensibility $L = 30$.

756 Initial gap size: 0.6mm, final gap size: 1.4mm, pistons relative velocity: 150mm/s.

757 Vertical line (---) corresponds to piston cessation of motion (aspect ratio 2.3).

758

759

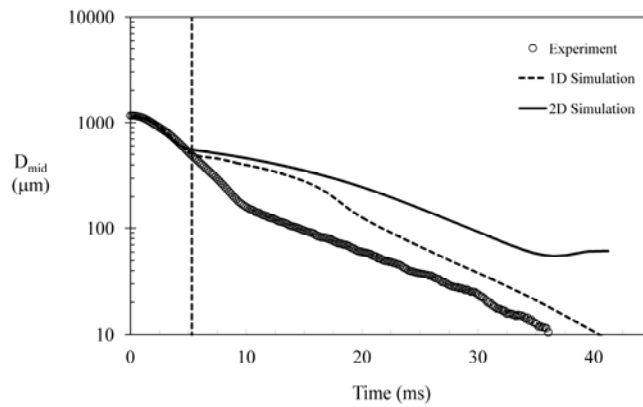


760

761 **Figure 9:** Single mode, 2.5wt% PS110 in DEP solution. Plot of the mid filament
762 diameter evolution as a function of time. Constitutive equation: Fene-CR, relaxation
763 time $\lambda = 1.19\text{ms}$, shear modulus $g = 15\text{Pa}$ and polymer extensibility $L = 30$. time (---)
764 corresponds to piston cessation of motion.

765

766

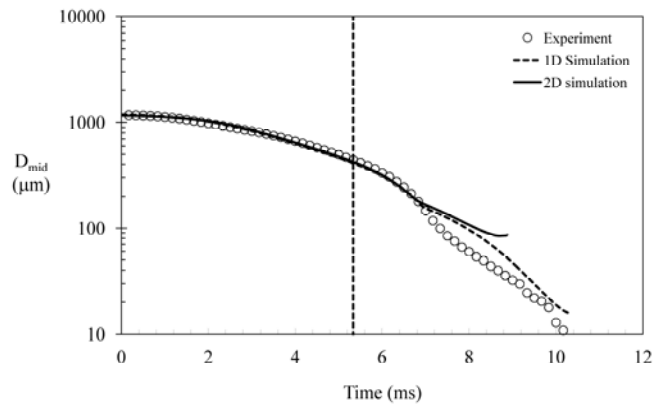


767

768 **Figure 10:** Single mode, 5wt% PS110 in DEP solution. Plot of the mid filament
 769 diameter evolution as a function of time. Constitutive equation: Fene-CR, relaxation
 770 time $\lambda = 3.2$ ms, shear modulus $g = 17$ Pa and polymer extensibility $L = 30$. Vertical
 771 Line (---) corresponds to piston cessation of motion.

772

773

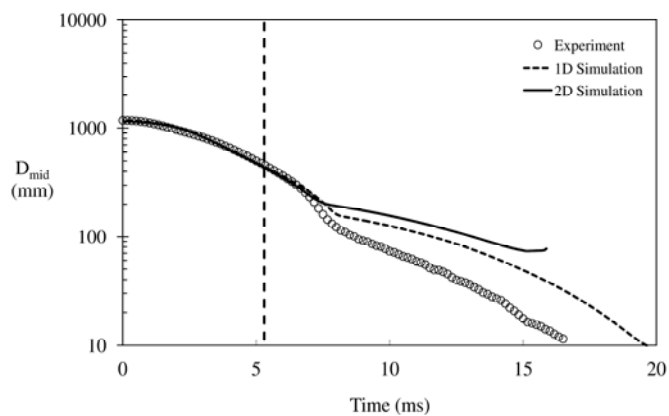


774
775

776 **Figure 11:** Multi mode, 1wt% PS110 in DEP solution. Plot of the mid filament
777 diameter evolution as a function of time. Constitutive equation: Fene-CR, relaxation
778 times λ_i and shear modulus g_i for the different modes i are given in Table II and
779 polymer extensibility $L = 30$. Vertical line (---) corresponds to piston cessation of
780 motion.

781

782

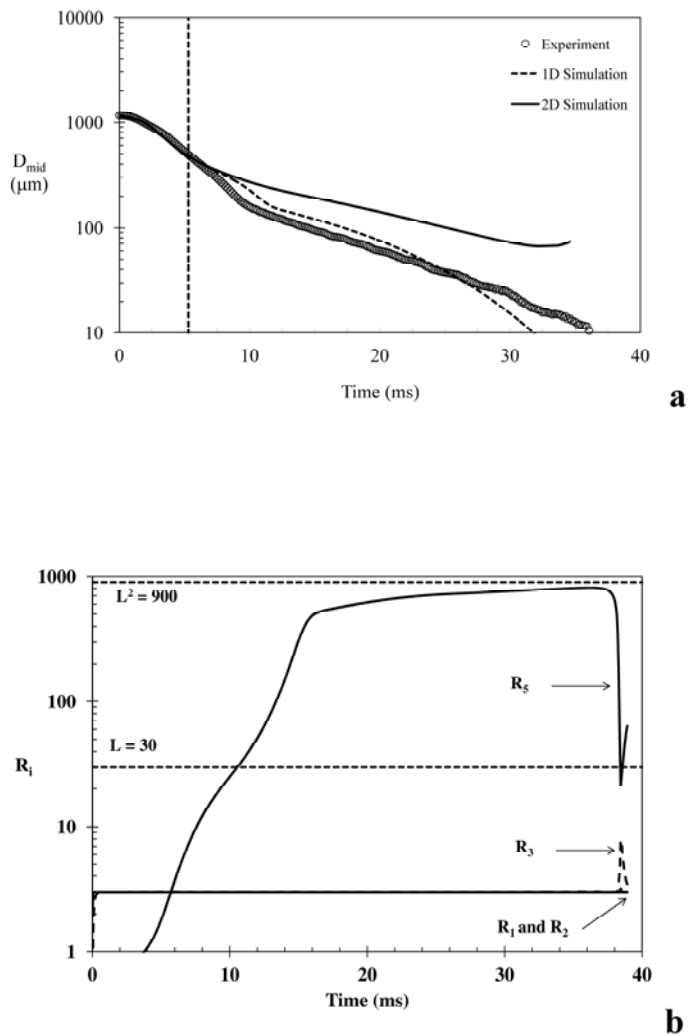


783

784 **Figure 12:** Multi mode, 2.5wt% PS110 in DEP solution. Plot of the mid filament
785 diameter evolution as a function of time. Constitutive equation: Fene-CR, relaxation
786 times λ_i and shear modulus g_i for the different modes i are given in Table II and
787 polymer extensibility $L = 30$. Vertical line (---) corresponds to piston cessation of
788 motion.

789

790



792

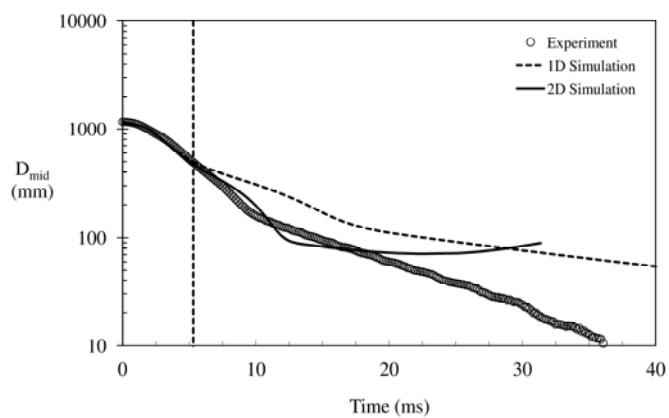
793 **Figure 13:** (a) Multi mode, 5% solution. Plot of the mid filament diameter evolution
 794 as a function of time. Constitutive equation: Fene-CR, relaxation times λ_i and shear
 795 modulus g_i for the different modes i are given in Table II and polymer extensibility L

796 = 30. Vertical line (---) corresponds to piston cessation of motion. (b) Evolution of

797 the R_i as a function of time

798

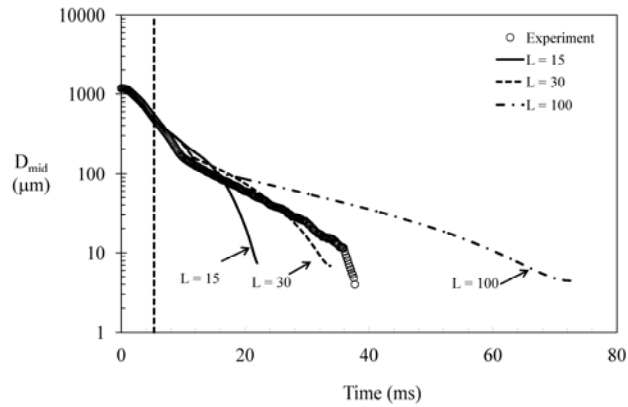
799



800

801 **Figure 14:** Multi modes, 5wt% PS110 in DEP solution. Plot of the mid filament
 802 diameter evolution as a function of time. Constitutive equation: Oldroyd-B, relaxation
 803 times λ_i and shear modulus g_i for the different modes i are given in Table II. Vertical
 804 line (---) corresponds to piston cessation of motion.

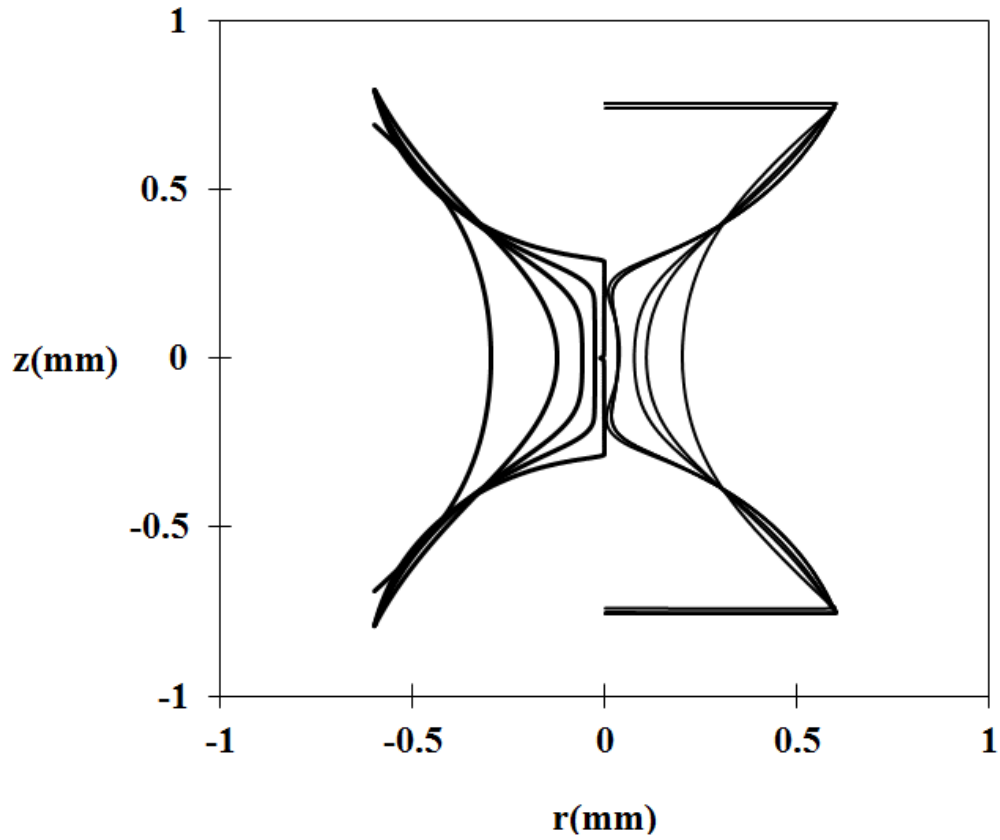
805



806

807 **Figure 15:** Effect of extensibility parameter L . Symbols represent the experimental
 808 data of the evolution of the mid-filament as a function time and lines represent 1D
 809 multi-mode numerical simulations for different polymer chain extensibilities L .
 810 Constitutive equation: Fene-CR , relaxation times λ_i and shear modulus g_i for the
 811 different modes i are given in Table II.. Vertical line (---) corresponds to piston
 812 cessation of motion.

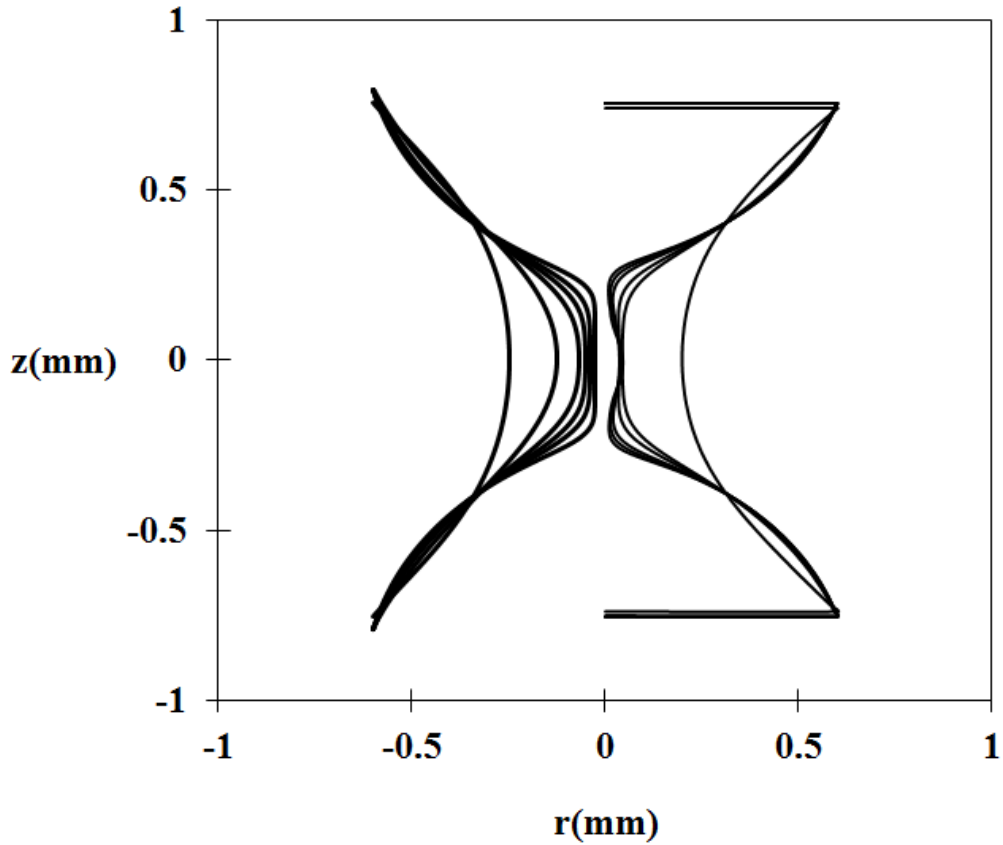
813



814
815

816 **Figure 16:** Comparison between the 1D numerical FENE-CR multimode transient
817 profiles (left), and the corresponding 2D simulations (right) for the DEP+5%PS. The
818 prescribed times are 5.3ms, 12ms, 18.5ms, 25.5 ms, 38ms.

819
820

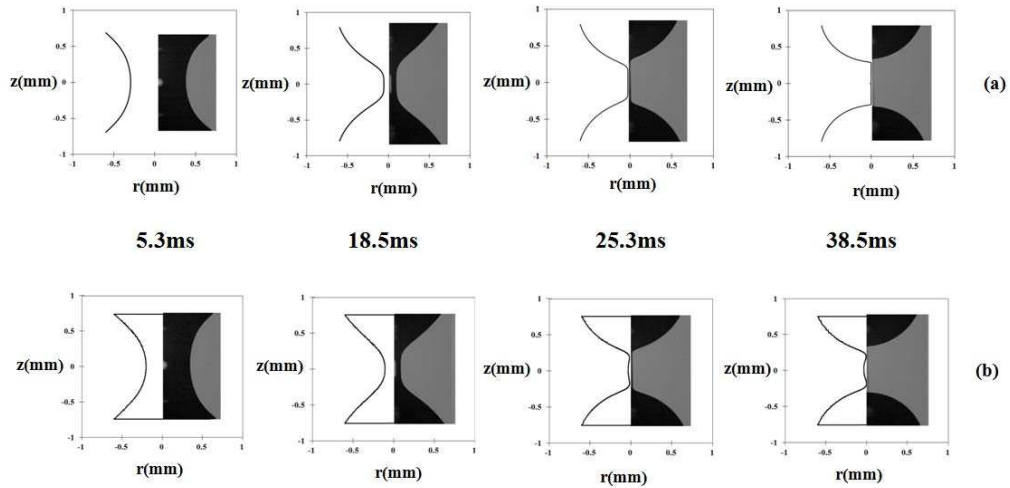


821

822 **Figure 17:** A comparison between the 1D numerical Oldroyd-B multimode transient
 823 profiles (left), and the corresponding 2D simulations (right). The prescribed times are
 824 5.3ms, 12ms, 18ms, 25ms, 32ms and 44ms for 1D simulation and 5.3ms, 12ms, 18ms,
 825 25ms, 28ms, 32.5ms for 2D simulation

826

827

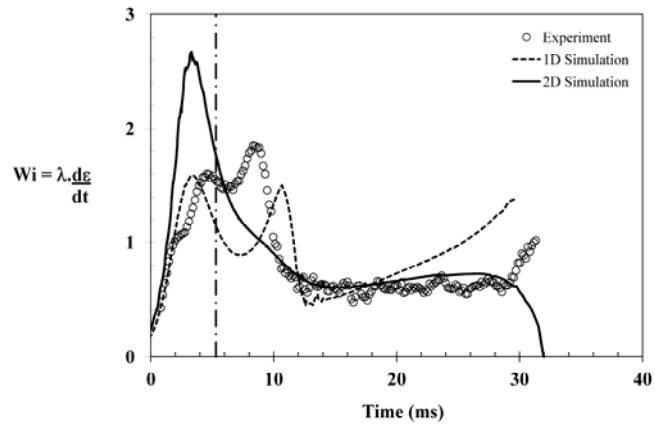


828

829 **Figure 18:** Comparison between the experimental transient profiles for the
 830 DEP+5wt%PS110 and the simulations of (a) the 1D and (b) the 2D cases using the
 831 FENE-CR multimode constitutive equations.

832

833



834

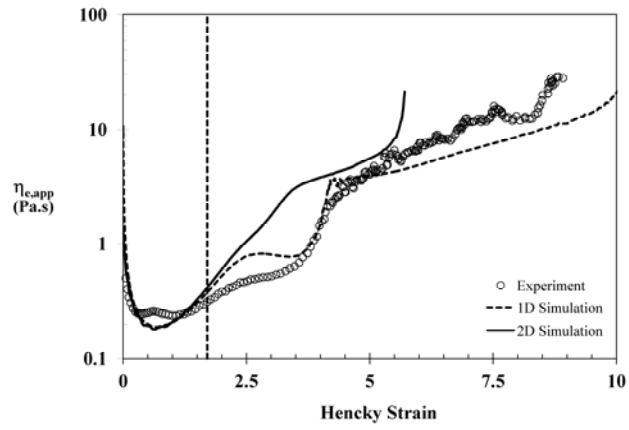
835 **Figure 19:** Evolution of the Weissenberg number as a function of the Hencky strain.

836 Transient Weissenberg numbers were calculated using $\lambda = 3.2\text{ms}$ for experimental

837 data, $\lambda = 2.89\text{ms}$ and $\lambda = 5.1\text{ms}$ for 1D simulation and 2D simulation data using multi

838 modes FENE-CR as constitutive equation.

839



840

841 **Figure 20:** Evolution of the transient apparent extensional viscosity $\eta_{e,app}$ as a
 842 function of the Hencky strain ϵ for computed from the mid filament evolution shown
 843 in Fig. 12.

844

845

846